# A new model for analyzing the effect of fractures on triaxial deformation

Wenlu Zhu*
Department of Geology and Geophysics
Woods Hole Oceanographic Institution
Woods Hole, MA 02543, USA

Joseph B. Walsh
Box 22, Adamsville, RI 02801, USA

*Corresponding author. wzhu@whoi.edu. 1-508-289-3355

**Abstract**

Rock is porous, with a connected network of cracks and pores. The static and dynamic behaviors of a rock sample under load depend on both the solid mineral matrix and the porous phase. In general, the configuration of the pore phase is complex; thus most studies on the effect of the porous phase on rock deformation are conducted numerically and theoretical analyses of the constitutive relations are scarce. We have studied rock deformation under axially-symmetric loading by analyzing a model where the pore phase is approximated by rough planes, randomly spaced and oriented, extending through the sample. The roughness is caused by asperities, all with the same tip radii, but having heights $h$ with a probability density distribution given by the negative exponential $e^{-h/\lambda}$ where $\lambda$ is a length parameter. Slip at contacts under local shear stress is resisted by simple Coulomb friction, with friction coefficient $f$. Both static and dynamic deformation were analyzed. The effect of porosity on deformation for both modes was found to be given by the non-dimensional parameter $\lambda\alpha_j$, where $\alpha_j$ is the total area of the fault planes per unit volume. We demonstrate that stress-induced microfracturing begins as randomly oriented microslip throughout the sample. As axial load increases, microslip occurs along preferred orientations and locations, which finally leads to deformation on a single fault. The model was found to fault under static loading conditions---the axial load at faulting and the angle of the "fracture" plane agree with values of those parameters given by Coulomb's theory of fracture. Dynamic moduli and Poisson's ratio are found to be virtually elastic and independent of the friction coefficient acting at contacts. The attenuation $Q_E^{-1}$ for uniaxial dynamic loading is a strong function of the friction coefficient and increases linearly with strain amplitude, in agreement with laboratory measurements.

**Keywords: Fractures**; Triaxial deformation; Roughness; Attenuation; Porosity

**Nomenclature**

$h, R$: height and radius of an asperity

$g(h/\lambda)$: probability density function of asperity heights, $g(h/\lambda)=e^{-h/\lambda}$, with $\lambda$ as a length parameter

$f$: frictional coefficient

$\alpha_j$: total area of the fault plane per unit volume

$\sigma_1, \sigma_2, \sigma_3$: principle stresses; axial stress $\sigma_1$ is equal to or greater than radial stress $\sigma_2$ and lateral stress $\sigma_3$ ($\sigma_1 \geq \sigma_2 = \sigma_3$) in an axis-symmetrical configuration.

$\beta$: the angle between a joint plane and the axial direction (1-axis); $\beta_\nu$ is the threshold value of $\beta$ above which no slip occurs on the joint and deformation is elastic

$p_0$: hydrostatic pressure

$\sigma, \tau$: normal and shear stresses acting on the joint surface; $\sigma_c, \tau_c$: normal and frictional shear stresses at asperities in contact

$\Delta$: change in stress or strain

$r$: ratio between change in $\sigma_3$ and change in $\sigma_1$, $r=\Delta\sigma_3/\Delta\sigma_1$, its maximum value is denoted as $r_m$

$\Delta w, \Delta u$: normal and shear displacements of a joint; $\Delta u^E$ consists of only the elastic contribution where no slip occurs along the joint; $\Delta u^S$ involves slip at asperity contacts

$\Delta u_1, \Delta u_3$: axial and radial displacements of a joint from both $\Delta w$ and $\Delta u$

$\Delta u_a, \Delta u_r$: total axial and radial displacements of a sample with a single joint; $\Delta u_a^M, \Delta u_r^M$ are the overall displacements for the solid matrix

$\varepsilon_a, \varepsilon_r$ : axial and radial strains of a sample with a single joint

$<\varepsilon_a>$, $<\varepsilon_r>$: overall axial and radial strains of a rock sample with randomly oriented joints;

$<\varepsilon_a>^M$, $<\varepsilon_r>^M$ are the axial and radial strains of the solid matrix

$\Delta W'$, $\Delta W''$: work done by the stresses

$L$, $L_j$ : lengths of the sample and of a joint $j$

$E$, $\nu$ : Young's modulus and Poisson's ratio of the elastic matrix

$\Delta \tilde{\sigma}_1$, $\Delta \tilde{\tau}$ ,: normal and shear cyclic stresses, $\Delta \tilde{\sigma}_1 / p_0 << 1$, and $\Delta \tilde{\tau} / p_0 << 1$

$\Delta \tilde{w}$, $\Delta \tilde{u}$ : normal and shear displacements of a joint resulting from small cyclic stress $\Delta \tilde{\sigma}_1$

$\Delta \tilde{u}_1$, $\Delta \tilde{u}_3$ : axial and radial displacements of a joint from $\Delta \tilde{w}$ and $\Delta \tilde{u}$

$\tilde{\varepsilon}_a$ , $\tilde{\varepsilon}_r$ : axial and radial strains of a sample with a single joint responding to dynamic loading

$< \tilde{\varepsilon}_a >$, $< \tilde{\varepsilon}_r >$: overall axial and radial strains of a rock sample with randomly oriented joints

responding to dynamic loading

$< \tilde{E} >$, $< \tilde{\nu} >$: Effective Young's modulus and Poisson's ratio of the sample

$\Delta \tilde{V} / V$ : volumetric strain

$< \tilde{K} >$: effective bulk modulus

$< \tilde{G} >$: effective shear modulus

$\Delta W_F$ : energy loss from friction for all planes

$\Delta W_{SE}$ : maximum strain energy

$Q_E^{-1}$: attenuation

$e$ : volumetric strain

$\Delta \sigma_{1F}$ , $\beta_F$ : asymptotic values of stress at large strain and the angle of faulting

$s_G$ , $s_E$ : slopes of a plot of $1/\tilde{G}$ vs. $1/p_0$ and a plot of $1/\tilde{E}$ vs. $1/p_0$

# 1. Introduction

Understanding the constitutive behavior of rocks deformed under crustal conditions is central to many civil engineering problems such as reservoir architecture, assessment of geological repositories for nuclear waste, drilling technology and energy recovery. All rocks of interest are porous to some degree----the range varies from sets of joints in natural rock formations to microcracks and tiny pores in hand specimens. We develop in the analysis here a procedure for calculating the overall elastic response of these porous structures to changes in applied loading, both static and dynamic. Clearly, not all possible distributions of joints or cracks can be considered, and so here we have applied the technique to rocks with random fractures. As we show, this model is a reasonable simulation of the behavior of intact rock, allowing theoretical results to be compared with published experimental data. Solid rocks include hard, crystalline rocks having porosity of the order of 1% to porous, sedimentary samples where the porosity may be 10% or more. The porous phase forms a connected network, and rock is found to be hydraulically and electrically conductive to depth in the earth of 30 km (e.g., [1]), with porosity serving as pathways. Rock has tensile strength, and so we know that the mineral phase is also continuous. Some pores in some rocks are not connected to the network, and undoubtedly fragments of the mineral ensemblage can be found isolated from the solid framework, but these aberrations do not have an appreciable effect on the mechanical properties that are of interest here.

The mechanical properties of rocks under crustal conditions are found in experiments to be nonlinear and hysteretic although deformation of the mineral framework is linearly elastic. Mathematical analysis (e.g., [2]) of models that simulate the structure of rock show that the nonelastic behavior can be explained by the closure of cracks under local normal stress and the

sliding of closed cracks against friction. The model used in these analyses consists of a linearly elastic body that contains cracks and also, in general, voids with more equant dimensions called pores. The cracks and pores are isolated in the matrix, and so existing solutions for the effect of voids having idealized shapes in an infinite medium can be used in the analyses. Although these analyses have been helpful in a qualitative sense for evaluating the effect of the porosity on mechanical properties, the model has several limitations. In the first place, quantitative evaluation is limited by the necessity of defining the "density" of isolated cracks and pores for a typical rock where porosity consists of a continuous network. In addition, the range of applied differential stresses that can be considered is limited by the microfracturing that can be expected, particularly at crack edges. Finally, the lack of connectivity between voids in the model is a serious defect when the transport properties such as fluid permeability and electric conductivity are to be studied.

We consider here a model where the pore phase is continuous and the mineral phase is not. In a fundamental sense, this is the model used in the various maximum-shear stress theories of faulting such as Coulomb-Navier criterion (e.g., [3]). In these theories, all planes through the body are considered to be planes of weakness, and elastic analysis is used to calculate the plane on which faulting eventually occurs---that is, the plane on which shear stress and normal stress reach the theoretical critical value. The analysis requires that the planes of weakness intersecting the body are only potential planes on which slip could occur; in fact, no slip does occur except on the fault plane at the instant of fracture, and elastic theory is valid throughout the body until fracture occurs.

Our model differs from those described above in that planes of weakness have no cohesive strength, and the body remains intact only because of the compressive loads acting on

it. The planes of weakness are assumed to be faults with rough surfaces. Relative displacements, both normal and shear, across the faults are possible because of deformation at asperities in contact. Deformation of the body as a whole therefore involves both the elastic deformation of the solid material between the faults and the relative shear and normal displacements across the faults. For the isotropic materials under consideration here, the faults are considered to be randomly spaced and oriented.

This model was used to analyze the behavior of porous rocks under hydrostatic pressure loading [4]. Because of the symmetry of the applied stress system, each fault in that analysis is subjected to a purely normal load. Although the matrix material can be assumed to be linearly elastic, the contribution of the joints to overall deformation is found to be non-linear, both because the Hertzian deformation of individual asperities is non-linear, and because the number of asperities contributing to the total load increases as closure brings them into contact. Walsh and Grosenbaugh's analysis [4] showed that the effective compressibility depends on porosity as described by the non-dimensional parameter $\alpha_j\lambda$, where $\alpha_j$ is the total area of the joints in the pore phase per unit volume and $\lambda$ is a characteristic length describing the topography of the joint surfaces. The significance of $\lambda$ will be discussed more fully later.

Walsh and Grosenbaugh [4] considered only the hydrostatic loading, analyzing effective bulk modulus by evaluating the response of each fault to normal stress alone and summing the contribution of all faults using an appropriate averaging scheme. In this study we use the same model to study deformation under triaxial loading, which is more relevant to engineering problems. Evaluation of elastic properties such as Young's modulus and Poisson's ratio requires summing the deformation at individual joints in both the normal and shear modes. These boundary conditions at the joint surfaces were established in a recent analysis [5] of the normal

and shear displacements for rough surfaces. Large overall displacements can be considered in our new model, and so all stages of deformation, from the initial elastic response to the final "fracture", can be analyzed. The passage of acoustic waves are also simulated by considering low amplitude, cyclic loading, giving expressions for both the elastic and the inelastic dynamic properties of the model.

## 2. Analysis

### 2.1 Preliminaries

As described above, porosity in isotropic rock is simulated by randomly oriented planar joints with rough surfaces intersecting an elastic body. We consider only axially-symmetric loading systems, as in Fig. 1. Because of this symmetry, a representative joint plane at angle $\beta$ to the 1-axis can be considered to be loaded by axial stress $\sigma_1$, lateral stress $\sigma_2$ applied parallel to the plane of the joint, and radial stress $\sigma_3$ ($\sigma_2=\sigma_3$) oriented normal to axial stress $\sigma_1$ and lateral stress $\sigma_2$, as in Fig. 2a. Lateral stress $\sigma_2$ doesn't affect deformation of the joint itself (although it contributes to the deformation of the elastic matrix), and so analysis of the effect of the joint on overall deformation of the body can be carried out considering only the axial and radial components, $\sigma_1$ and $\sigma_3$, respectively, of the loading system, as in Fig. 2b. As shown in Fig. 2b, the applied loads $\sigma_1$ and $\sigma_3$ are equilibrated by normal and frictional shear stresses, $\sigma_c$ and $\tau_c$, at the interface between asperities in contact.

In typical "triaxial" tests in the laboratory, a hydrostatic pressure $p_0$ is applied to the sample, and this is considered the initial state for subsequent changes in stresses and displacements. Accordingly, we adopt the notation that changes in stresses and displacements are indicated by $\Delta$; for example:

$$\Delta\sigma_1 = \sigma_1 - p_0$$
$$\Delta\sigma_3 = \sigma_3 - p_0 \tag{1}$$
$$\Delta\sigma = \sigma - p_0$$

as in Fig. 3. We will be analyzing cases where the change $\Delta\sigma_3$ in radial stress is proportional to

the change $\Delta\sigma_1$ in axial load, that is

$$\Delta\sigma_3 = r\Delta\sigma_1 . \tag{2}$$

Using Mohr's construction, we find that applied stresses $(\sigma, \tau)$ acting on the joint surface

are

$$\tau = \Delta\sigma_1(1-r)\sin\beta\cos\beta$$
$$\sigma = r\Delta\sigma_1 + p_0 + \Delta\sigma_1(1-r)\sin^2\beta \tag{3}$$

This applied stress system is in equilibrium with shear and normal stresses, $\sigma_c$ and $\tau_c$, at contacts

(as in Fig. 2b). The deformation of the surface to this stress system---both the normal and shear

components of joint deformation $(\Delta w, \Delta u)$---depends on the topography of the surfaces in

contact. The topography of the microfractures that comprise porosity isn't known, of course, but

fortunately the simple model proposed by Greenwood and Williamson [6] has been found to

provide a good simulation for a variety of fault surfaces [7]. We assume that it is adequate for the

analysis here. Greenwood and Williamson [6] assume that asperities are so widely spaced that

deformation at one location does not affect neighboring contacts. Further, the tips of all asperities

are assumed to have the same radius $R$, and the probability density function $g(h)$ for heights $h$

(relative to a fixed plane through the rough surface) is approximated by a negative exponential,

that is

$$g(h/\lambda) = e^{-h/\lambda} \tag{4}$$

In a previous analysis [5], we show that the normal and shear displacements $(\Delta w, \Delta u)$ for

this model of a rough surface are given by the expressions:

$$\Delta w/\lambda = \ln(\sigma/p_0)$$
$$-(\Delta u^S/f\lambda) = \ln(1-\tau/f\sigma) \tag{5}$$

where the assumption has been made that $2(1-\nu)/(2-\nu) \approx 1$; this approximation induces an error of 20% at most for typical values of Poisson's ratio $\nu$. The superscript $S$ in (5) indicates that shear displacement $\Delta u^S$ involves slip at asperity contacts. Walsh and Zhu [5] show that for slip to occur

$$\tau \geq f\Delta\sigma. \tag{6}$$

For planes oriented such that shear stress $\tau$ is less than $f\Delta\sigma$, contacts are "locked", and so the shear deformation that occurs is elastic; i.e., the component resulting from slip at contacts is zero. The elastic displacement $(\Delta u^E/\lambda)$ for a locked surface is found by examining the expression for $(\Delta u^S/\lambda)$ in (5) in the limit where slip is no longer possible; this can be done, for example, by allowing the friction coefficient to become infinite. We find that displacements at the joint are given by

$$\Delta w/\lambda = \ln(\sigma/p_0) \qquad (0 \leq \beta \leq \pi/2)$$
$$-(\Delta u^S/f\lambda) = \ln(1-\tau/f\sigma) \qquad (0 \leq \beta \leq \beta_\upsilon) \tag{7}$$
$$(\Delta u^E/\lambda) = \tau/\sigma \qquad (\beta_\upsilon \leq \beta \leq \pi/2)$$

where $\beta_\upsilon$ is the angle that separates planes on which slip occurs from those on which deformation is elastic.

Introducing (1) and (3) into (6), we find that $\beta_\upsilon$ is described by the relationship

$$(1-r)\sin\beta_\upsilon \cos\beta_\upsilon = \left[ r + (1-r)\sin^2\beta_\upsilon \right]/f$$

or

$$\tan^2\beta_\upsilon - (\frac{1-r}{f})\tan\beta_\upsilon + r = 0 \tag{8}$$

Factoring (8), we find

$$\tan \beta_\upsilon = \frac{1}{2}\left[(\frac{1-r}{f}) \pm \sqrt{(\frac{1-r}{f})^2 - 4r}\right] \qquad (9a)$$

Evaluating (9a) for the case of uniaxial compression ($r=0$) shows that the $+$ sign before the radical is operative; i.e.,

$$\tan \beta_\upsilon = \frac{1}{2}\left[(\frac{1-r}{f}) + \sqrt{(\frac{1-r}{f})^2 - 4r}\right] \qquad (9b)$$

Note in (9b) that for a specified friction coefficient $f$, $r$ has a limited range over which slip ($\Delta u/f\lambda$) in (7) is possible; that is, $r$ has the maximum value $r_m$ such that the radical is not negative:

$$\sqrt{\left(\frac{1-r_m}{f}\right)^2 - 4r_m} = 0 \qquad (10a)$$

Making use of the binomial theorem, we find

$$r_m = 1 + 2f^2 - 2f\sqrt{1+f^2} = (\sqrt{1+f^2} - f)^2 \qquad (10b)$$

and the range of angles for which slip can occur is found from (9b) and (10b). It can be expressed as

$$\tan \beta_\upsilon \le \sqrt{1+f^2} - f = \sqrt{r_m}. \qquad (10c)$$

*2.2 Reciprocal Theorem*

Betti's reciprocal theorem [8] provides a convenient method for evaluating the effect of the deformation of the model's two components---the joints and the solid, elastic matrix---on overall deformation of the body. The technique involves the use of two stress systems acting individually on bodies having the same configuration and elastic properties. The two stress systems are illustrated in Fig. 4. Fig. 4a describes the actual stresses and displacements for the model that we are using (as in Figs. 2 and 3). The other stress system is designed such that

application of the reciprocal theorem will produce the characteristics of the body one is seeking.

Here we need the overall deformation resulting from the radially symmetric stress system ($\Delta\sigma_1$, $r\Delta\sigma_1$). To derive the axial component of the displacement, we apply an axial stress to the external and internal surfaces of the body; as in Fig. 4b, this results in a uniform stress throughout the body.

In its simplest form, the reciprocal theorem demonstrates that the work $\Delta W'$ done by the stresses in Fig. 4a acting through the displacements in Fig. 4b must equal the work $\Delta W''$ done by the stresses in Fig. 4b acting through the displacements in Fig. 4a. The displacements $\Delta u_1$ and $\Delta u_3$ in the axial and radial directions from the components $\Delta w$ and $\Delta u$ normal to and parallel with the joint surface are given by (5); referring to Fig. 5, we find,

$$\begin{aligned} \Delta u_1 &= \Delta u \cos\beta + \Delta w \sin\beta \\ \Delta u_3 &= -\Delta u \sin\beta + \Delta w \cos\beta \end{aligned} \tag{11}$$

Note that $\Delta u_1$ and $\Delta u_3$ are positive in compression (shortening). The displacements $\Delta u$ and $\Delta w$ in (5) are expressed in terms of stresses $\Delta\sigma_1$ and $r\Delta\sigma_1$, in the axial and radial directions by combining (3) and (7); incorporating the restrictions imposed by (9b) gives

$$\begin{aligned} \Delta w/\lambda &= \ln\left\{1 + (\Delta\sigma_1/p_0)[r + (1-r)\sin^2\beta]\right\} & \\ \Delta u^S/\lambda &= f \ln\left\{\frac{1 + (\Delta\sigma_1/p_0)[r + (1-r)\sin^2\beta]}{1 + (\Delta\sigma_1/p_0)[r + (1-r)\sin^2\beta(f - \cot\beta)/f]}\right\} & 0 \le \beta \le \beta_\upsilon \\ \Delta u^E/\lambda &= \frac{(\Delta\sigma_1/p_0)[(1-r)\sin\beta\cos\beta]}{1 + (\Delta\sigma_1/p_0)[r + (1-r)\sin^2\beta]} & \beta_\upsilon \le \beta \le \pi/2 \end{aligned} \tag{12}$$

Displacements at the joint in Fig. (4b) are found to introduce terms of the order of porosity; such terms are negligible in an analysis like this, and so we ignore these displacements in the calculation. Work $\Delta W'$ is found to be give by the expression

$$\Delta W' = (\Delta\sigma_1^2 / E)L^3(1 - 2r\nu) \tag{13a}$$

The expression for $\Delta W''$ is found to be

$$\Delta W'' = \Delta\sigma_1 (L^2 \Delta u_a - L_j^2 \sin\beta \Delta u_1) \tag{13b}$$

where $L_j$ is the length of the joint, and $L_j \sin\beta$ is the length of the joint normal to the axis of symmetry.

Evaluating (13a) and (13b), we find

$$\varepsilon_a = \varepsilon_a^M + \alpha_j \sin\beta \Delta u_1 \tag{14a}$$

where $\varepsilon_a = \Delta u_a / L$

$$\varepsilon_a^M = (\Delta\sigma_1 / E)(1 - 2r\nu)$$

$$\alpha_j = \text{joint area per unit volume} = L_j^2/L^3,$$

superscript $M$ refers to elastic properties of the solid matrix, and $\Delta u_1$ is given by (11) and (12).

The effective displacement $\Delta u_r$ in the radial direction is found following the same procedure, except that $\Delta\sigma_3$ is applied to all internal surfaces as well as the external radial faces. One finds that the radial strain $\varepsilon_r$ is given by the expression

$$\varepsilon_r = \varepsilon_r^M + (\alpha_j / 2)\cos\beta \Delta u_3 \tag{14b}$$

where $\varepsilon_r = \Delta u_r / L$

$$\varepsilon_r^M = -(\Delta\sigma_1 / E)[\nu - r(1 - \nu)]$$

and $\Delta u_3$ is given by (11) and (12).

The deformation of the body as a whole is found by summing the contribution of each joint plane defined by (14), given the constraints in (9). We are considering isotropic behavior, and so the joint planes must be randomly oriented; the procedure for assuring that the distribution is random is to consider each positioned uniformly on the surface of a unit sphere, as

in Fig. 6. We see that the summations for overall axial and radial strains $<\varepsilon_a>$ and $<\varepsilon_r>$ are given by the integrals

$$< \varepsilon_a > -\varepsilon_1^M = \alpha_j \lambda \{ \int_0^{\beta_\upsilon} \frac{\Delta u^S}{\lambda} \sin\beta \cos^2\beta d\beta + \int_{\beta_\upsilon}^{\pi/2} \frac{\Delta u^E}{\lambda} \sin\beta \cos^2\beta d\beta + \int_0^{\pi/2} \frac{\Delta w}{\lambda} \sin^2\beta \cos\beta d\beta \}$$

$$< \varepsilon_a > -\varepsilon_r^M = (\alpha_j \lambda/2) \{ -\int_0^{\beta_\upsilon} \frac{\Delta u^S}{\lambda} \sin\beta \cos^2\beta d\beta - \int_{\beta_\upsilon}^{\pi/2} \frac{\Delta u^E}{\lambda} \sin\beta \cos^2\beta d\beta + \int_0^{\pi/2} \frac{\Delta w}{\lambda} \cos^3\beta d\beta \}$$

(15)

The integrals were evaluated using MATHEMATICA and plots of $< \varepsilon_a > -\varepsilon_a^M$ and $< \varepsilon_r > -\varepsilon_r^M$ are given in Fig. 7. Of course, all rocks are anisotropic to various degrees. The effect of anisotropy on rock deformation can be incorporated into expression (15) by including weighting functions in the integration. These weighting functions should represent the statistical distribution of voids obtained by quantitative structural or microstructural study.

*2.3 Dynamic Stressing---Elastic Component*

A stress wave traversing a sample superimposes a harmonically varying stress on the existing stress system. Mindlin and Deresiewicz [9] show for a single asperity that cyclic loading is almost elastic at small amplitudes, and further that the compliance of the contact to cyclic loading does not depend on the shear stress acting on the joint. Walsh [7] found that these observations held as well for rough surfaces.

On the other hand, dynamic compliance does depend on the normal stress, as one would expect: higher normal stress increases the area of contacts and the number of contacts, making the surface stiffer. It is this sensitivity of compliance to normal stress that gives rise to "stress induced anisotropy" and "shear wave birefringence" observed in experiments on isotropic samples where the background stress system is not hydrostatic. Intrinsic anisotropy in the porous structure, and anisotropy caused by stressing, can be accommodated in the model we have proposed, but such topics are not warranted in the analysis here, where general characterization

of constitutive behavior is of interest. Accordingly, we assume that dynamic loading is superimposed on an isotropic system; i.e., the sample is structurally isotropic and the pre-existing stress is hydrostatic.

We find the elastic dynamic response by repeating the analysis for small excursions in the cyclic axial stress $\Delta\tilde{\sigma}_1$; i.e., for $\Delta\tilde{\sigma}_1 / p_0 << 1$. Normal and shear displacements $\Delta\tilde{w}/\lambda$ and $\Delta\tilde{u}/\lambda$ of the joint for $\Delta\tilde{\sigma}_1 / p_0 << 1$ are found from (12) to be given by the expressions

$$\Delta\tilde{w}/\lambda = (\Delta\tilde{\sigma}_1 / p_0)[r + (1-r)\sin^2\beta]$$
$$\Delta\tilde{u}/\lambda = (\Delta\tilde{\sigma}_1 / p_0)(1-r)\sin\beta\cos\beta \tag{16}$$

Axial and radial displacements of the joint, $\Delta\tilde{u}_1$ and $\Delta\tilde{u}_3$, are found from (11) and (16) to be

$$\Delta\tilde{u}_1 / \lambda = (\Delta\tilde{\sigma}_1 / p_0)\sin\beta$$
$$\Delta\tilde{u}_3 / \lambda = r(\Delta\tilde{\sigma}_1 / p_0)\cos\beta$$

and $\tilde{\varepsilon}_a$ and $\tilde{\varepsilon}_r$ from (14) are expressed by

$$\tilde{\varepsilon}_a - \varepsilon_a^M = \alpha_j\lambda(\Delta\tilde{\sigma}_1 / p_0)\sin^2\beta$$
$$\tilde{\varepsilon}_r - \varepsilon_r^M = r(\alpha_j\lambda/2)(\Delta\tilde{\sigma}_1 / p_0)\cos^2\beta \tag{17}$$

Strains in (17) are elastic (note that friction factor $f$ does not appear), and so integration is over all orientations $0\leq\beta\leq\pi/2$; we find

$$<\tilde{\varepsilon}_a> -\varepsilon_a^M = (\alpha_j\lambda/3)(\Delta\tilde{\sigma}_1 / p_0)$$
$$<\tilde{\varepsilon}_r> -\varepsilon_r^M = r(\alpha_j\lambda/3)(\Delta\tilde{\sigma}_1 / p_0) \tag{18}$$

Young's modulus $<\tilde{E}>$ is given by $\Delta\tilde{\sigma}_1 / <\tilde{\varepsilon}_a>$, and Poisson's $<\tilde{v}>$ ratio is $-<\tilde{\varepsilon}_r> / <\tilde{\varepsilon}_a>$. For uniaxial compression ($r$=0); we find from (18)

$$1/ <\tilde{E}> -1/ E^M = (\alpha_j\lambda/3)(1/ p_0)$$
$$<\tilde{v}> = -v^M /[1 + (\alpha_j\lambda/3)(E^M / p_0)] \tag{19}$$

Note that the response to a purely hydrostatic cyclic loading can be found from (19). The sample is subjected to a uniform harmonic hydrostatic load by letting $r=1$ in (18); the volumetric strain $\Delta \tilde{V} / V$ is given by

$$\Delta \tilde{V} / V = <\tilde{\varepsilon}_a> +2 <\tilde{\varepsilon}_r>, \text{ or}$$

$$1/<\tilde{K}> = 1/K^M + \alpha_j \lambda / p_0 \tag{20}$$

where $<\tilde{K}> = \Delta\tilde{\sigma}/<\Delta\tilde{V}/V>$.

Note also that, because the sample can be considered elastic for small amplitude cyclic loading, dynamic behavior under shear loading can be found from (18) and (19) using the standard relationships between elastic properties; for example, effective shear modulus $<\tilde{G}>$ can be evaluated from the relationship

$$1/<\tilde{G}> = 3/<\tilde{E}> -1/3<\tilde{K}>,$$

giving

$$1/<\tilde{G}> = 1/G^M + 2\alpha_j \lambda / 3p_0 \tag{21}$$

*2.4 Dynamic Stressing---Anelastic Component*

Although the sample can be considered to be elastic for small amplitude cyclic loading, nevertheless some energy is dissipated owing to micro-slip against friction at some contacts. Although all contacts contribute to the stiffness of the surface, not all contacts are a source of frictional dissipation. As we saw in the analysis for the static constitutive behavior of the model, deformation on planes having certain orientations given by (9) is purely elastic. Here, to simplify the presentation, we consider only the case $r=0$, i.e., the cyclic loading is uniaxial compression $\Delta\tilde{\sigma}_1$, where $\Delta\tilde{\sigma}_1 / p_0 << 1$.

Mindlin and Deresiewicz [9] derived an expression giving the energy loss for this case resulting from frictional dissipation for two asperities in contact. Deriving the expression for the loss $\Delta W_F$ from friction for all planes involves summing the contribution from each joint for which loss occurs. Referring to the Appendix, we see that the analysis is straightforward, following the same steps leading to the expression for $<\tilde{E}>$ in (19). The loss $\Delta W_F$ per unit volume arising from frictional dissipation given by (A-7) is found to be

$$\Delta W_F = \frac{4}{3}\left[\frac{2-\nu}{2(1-\nu)}\right]\alpha_j\lambda(\Delta\tilde{\sigma}_1^3 / p_0^2)F(\beta_\upsilon),$$

where

$$F(\beta_\upsilon) = \int_0^{\beta_\upsilon}(1/f)(1-f^2\tan^2\beta)\sin^4\beta\cos^4\beta d\beta \tag{22}$$

$F(\beta_\upsilon)$ was calculated numerically and is plotted in Fig. 9.

Attenuation in dissipative materials is commonly described by $Q^{-1}$, the reciprocal of the quality factor. For uniaxial compression, the attenuation $Q_E^{-1}$ is

$$Q_E^{-1} = (1/2\pi)(\Delta W_F / \Delta W_{SE}) \tag{23a}$$

where $\Delta W_F$ is the energy loss per cycle and $\Delta W_{SE}$, the maximum shear strain energy during the cycle, is

$$\Delta W_{SE} = \Delta\tilde{\sigma}_1^2/2<\tilde{E}> \tag{23b}$$

Combining (22) and (23) gives

$$Q_E^{-1} = \frac{4}{3\pi}\left[\frac{2-\nu}{2(1-\nu)}\right]\alpha_j\lambda(<\tilde{E}>/p_0)^2\Delta\tilde{\varepsilon}F_E(\beta_\upsilon) \tag{24}$$

where

$$\Delta\tilde{\varepsilon} = \Delta\tilde{\sigma}/<\tilde{E}> \tag{25}$$

## 3. Discussion

We have analyzed a model for simulating the deformation of rocks under stress in which the pore space is the aperture between rough faults traversing the sample. For the isotropic material considered here, the faults are randomly spaced and oriented. As in a previous analysis [4], employing this model, the effect of porosity is found to be described by the non-dimensional term, $\lambda\alpha_j$, where $\alpha_j$ is the area of all joints per unit volume and $\lambda$ is a parameter having dimensions of length that describes the roughness of the surface in a statistical sense.

The topography of most rough surfaces can be described statistically as Gaussian ($g(h/\lambda) = \dfrac{1}{\sqrt{2\pi}} e^{-(h/\lambda)^2/2}$); that is, the heights of the surface above a reference plane at random locations have a normal distribution. Here, we are interested in the distribution of the heights of asperities (summits) above the reference plane. This distribution can be found [10-12] from the first three moments of underlying distribution of heights. To make the calculations easier, we have chosen to approximate the distribution $g(h/\lambda)$ of asperity heights $h$ by a negative exponential $e^{-h/\lambda}$ (see (4)), where $\lambda$ is found by fitting the exponential to the appropriate part of the distribution function. We make the further simplification that all asperities have the same tip radius $R$. The justification for using these approximations and the procedure for estimating $\lambda$ are discussed by Walsh [7].

We have considered only applied stress systems that are axially symmetric; i.e., deformation occurs in response to an axial stress $\sigma_1$ and radial stress $\sigma_3$. Overall deformation is composed of components representing elastic compression of the solid material in the model and closure of the rough faults comprising the pore phase. Although the matrix material is linearly elastic, deformation in the model is non-linear because closure and slip against friction at the

joints isn't a linear process. In this respect, the model is similar to models where pore space consists of isolated pores and cracks----in these models, closure and slip against friction at cracks introduces the non-linear element of overall deformation, which is characteristic of rock deformation observed in the laboratory.

Summing the contributions of all of the individual components of the body is conveniently carried out using the reciprocal theorem. The procedure, which is described briefly in the text, leads to general expressions (14) for axial and radial strains ($\varepsilon_a$, $\varepsilon_r$) involving the non-dimensional parameter $\lambda\alpha_j$ that describes the configuration of the pore phase, the friction coefficient $f$, and the ratio $r$ of the applied radial stress $\Delta\sigma_3$ to the axial value $\Delta\sigma_1$ (see (1) and (2)). The integrations required to evaluate (14) were carried out numerically using MATHEMATICA, and the results are presented in graphical form in Fig. 7.

*3.1 Triaxial Experiments*

The constitutive behavior of the model in experiments where radial stress $\Delta\sigma_3$ is increased at a uniform rate $r$ proportional to the axial load $\Delta\sigma_1$ is described in Fig. 7. We see that, in general, strains are a function of both the ratio $r$ ($=\Delta\sigma_3/\Delta\sigma_1$) and the Coulomb friction coefficient $f$. The volumetric strain $e$, where

$$e = \varepsilon_a + 2\varepsilon_r, \tag{26}$$

is anomalous. Calculating $e$ from (15), we find

$$e = e^M + \int_0^{\pi/2}(\Delta w/\lambda)\cos\beta \, d\beta \tag{27}$$

Note that the expression for $e$ in (27) depends only on the normal displacement $\Delta w$ between the fractures; it is unaffected by the friction coefficient $f$, and so the volumetric strain component can be expected to be free from dissipation and hysteresis in loading/unloading cycles.

The expression for volumetric strain $e$ in (27) can be integrated [13, eqn. 2.733.1], giving a solution in closed form:

$$e = e^M + \alpha_j \lambda \{\ln(1 + \Delta\sigma_1 / p_0) - 2[1 - S \tan^{-1}(1/S)]\}$$

where

$$S = \sqrt{\left(1 + \frac{\Delta\sigma_1}{p_0} r\right) \Big/ \frac{\Delta\sigma_1}{p_0}(1 - r)} \qquad (28)$$

As $r$ approaches one (as the load approaches uniform compression), (28) becomes

$$e - e^M = \alpha_j \lambda \ln(1 + \Delta\sigma_1 / p_0) \qquad (29)$$

Note that (29) could be obtained directly from (12) for $r=1$ and (14).

Walsh and Grosenbaugh [4] analyzed the deformation of cracked elastic bodies under hydrostatic pressure, and Wong et al. [14] refined the calculation. As in the present model, fractures were considered to be rough surfaces with asperity heights distributed as in (4), with the difference that fractures did not necessarily extend through the body. The compressibility of their model at zero load is finite, therefore, where as in the present model the compressibility is infinite. Allowing for this difference, one can show that all expressions are equivalent for the case where compressibility under zero load is infinite.

As mentioned above, the lack of a term involving friction in the general expression for volumetric strain suggests that no hysteresis should be observed in a plot of volumetric strain during a loading/unloading cycle under any loading path. Walsh [2] analyzed a uniaxial compression test on Westerly granite in which axial and radial strains were measured throughout a loading/unloading cycle. Although hysteresis was observed in stress-strain curves for both axial and radial components, hysteresis was negligible in a plot of volumetric strain as a function

of stress, in agreement with the analysis here (and in Walsh's [2] analysis of a model utilizing open and closed ellipsoidal cracks).

*3.2 Faulting*

The constitutive behavior of the model in a conventional uniaxial compression experiment (i.e., where $r=0$) is described in Fig. 7a. We see in Fig. 7a, that uniaxial stress approaches an asymptotic value $\Delta\sigma_{1F}$ at large strains for all values of friction coefficient $f$ (except $f=\infty$ where contacts are effectively welded). The value of $\Delta\sigma_{1F}$ can be calculated using (12). Note in (12) that the expression for $u^S/\lambda$ approaches infinity as the denominator approaches zero. That is, the asymptotic values of the angle $\beta_F$ of faulting and stress $\Delta\sigma_{1F}$ can be found from the equation

$$0 = 1 - \left(\frac{\Delta\sigma_1}{p_0}\right)_j \left\{(1-r)\left[\sin^2\beta(\cot\beta - f)/f\right] - r\right\}_j \tag{30}$$

In a conventional triaxial experiment, $r=0$, and (30) becomes

$$\left(\frac{\Delta\sigma_1}{p_0}\right)_j \left[(\sin\beta\cos\beta/f) - \sin^2\beta\right] = 1$$

or equivalently,

$$\left(\frac{\Delta\sigma_1}{p_0}\right)_j \left[(\sin 2\beta/f) + \cos 2\beta - 1\right] = 2 \tag{31}$$

The asymptotic values of $\Delta\sigma_1/p_0$ depend on $\beta$, and the value $(\Delta\sigma_{1F}/p_0)$ operative in the model is the minimum value; that is, the value where $d(\Delta\sigma_1/p_0)/d\beta=0$. We find from (31) that the angle $\beta_F$ for faulting is given by the expression

$$\tan 2\beta_F = 1/f \tag{32}$$

and the value $\Delta\sigma_{1F}$ of axial stress at faulting is given by

$$(\Delta\sigma_{1F} / p_0)_j = 2f(f + \sqrt{1 + f^2}) \tag{33}$$

It is interesting to note that (32) and (33) are the expressions that define the axial stress required for faulting and the angle of the fault in Coulomb's (and others) theory of failure (see [3]) for the special case where the strength at zero confining pressure is zero. We see that the model provides an alternate way of arriving at theoretical failure stress, namely by determining displacements and deriving the stress and angle for which slip displacement is unlimited. The similarity between the behavior of the model and the maximum shear stress theory of faulting isn't exact because in faulting theory fracture occurs by failure along a single plane, whereas in the model failure occurs by uninhibited sliding along many planes symmetrically positioned around the axis. In addition, as noted above, the model has no strength until compressive stresses are applied, whereas faulting theory provides for a finite tensile strength, which, of course, is characteristic of real rock. (Analyzing a model where the fracture planes don't extend completely through the body involves only minor variations in the analysis presented here; we didn't use this approach, however, because we felt the advantages were small compared with the complications that it increased in the calculations and presentation of the results).

One finds by following the same procedure outlined above for the case where $r \neq 1$ in expression (30) that faulting occurs only for a limited range of $r$ and $f$. Repeating the calculations here would be superfluous; they show, surprisingly, that the angle $\beta_F$ at which faulting occurs does not depend on $r$; i.e., $\beta_F$ is given by (32). The faulting stress $(\Delta\sigma_{1F} / p_0)$ is found to be given by the expression

$$\Delta\sigma_{1F} / p_0 = \left[ \left( \frac{1-r}{2} \right)\left( \frac{1}{f} \right)\sqrt{1 + f^2} - \left( \frac{1+r}{2} \right) \right]^{-1} \tag{34}$$

Note in (34) that faulting stress $\Delta\sigma_{1F}$ becomes infinite when the term in brackets is zero. In other words, for a given radial stress ratio $r$, faulting occurs only for a range of values for friction coefficient $f$ given by

$$f^2 \leq (1-r)^2 / 4r \tag{35}$$

The failure of real rock occurs in stages, and some rocks under some conditions may not fail by brittle faulting at all----i.e., the specimen can support higher and higher axial loads with no instability or asymptotic limit. Generally speaking, strong, low-porosity rocks fail by faulting at all confining pressures attainable in the laboratory, whereas weaker, higher-porosity rocks fault only at relatively low confining pressures (e.g., [15-17]). Deformation in this class of rocks at low axial stress is elastic, or nearly so. Though elastic, the stress-strain curve is concave upwards (i.e., becomes stiffer under increasing load) because of the non-linear effect of the compression of pore space, as described above. Measurements of acoustic emission (e.g., [18]) show that microfracturing begins as axial stress is increased, the events positioned and oriented randomly throughout the sample. As axial load increases, these events begin to show a preferred orientation and location, and finally the sample fails by faulting on the plane described by these latter events.

Our model simulates in an approximate way the initial and final steps in this process. In Fig. 7, we have plotted a curve labeled $f=\infty$; for this case, contacts are effectively welded, and so the sample responds elastically, with no fracturing. As described above, the other curves refer to a sample where all contacts are mobile. One can imagine simulating the deformation of a real rock as a gradual transition from elastic response (i.e., $f=\infty$) to faulting and pre-faulting behavior of the model when contacts are free to slide. We illustrate the progress from microfracturing to faulting in Fig.8. The elastic phase 0-1 during brittle failure of a rock can be simulated in the

model by letting the friction coefficient become infinite: deformation arises only from closing of the pore phase. In the leg 1-2 where microfracturing is ubiquitous, we allow the friction coefficient to assume a finite value: microfracturing is equivalent to slip occurring at contacts on the rough surfaces which comprise the pore phase. Microfracturing in leg 2-3 occurs preferentially along the future plane of faulting. We could simulate this stage by analyzing a model where slip on a particular plane is enhanced by, for example, assuming that the geometric factor $\lambda \alpha_j$ is larger for that orientation. But such a calculation is beyond the scope of this study, so we have merely indicated in Fig.8 a transition to deformation on a single fault in leg 3-4.

In Fig. 8, we see that the deformation path we have sketched is energetically acceptable, that is, the elastic strain energy released from stress reduction under increasing strain is available to balance energy lost through sliding against friction. Although the progression from elastic deformation to faulting in Fig.8 is observed for some rocks, the energy balance lacks one significant component, namely work done by volume change acting against confining pressure. By assuming that displacements are continuous throughout the body and no gaps open up as slip occurs on fracture planes, our model ignores one characteristic of deformation in the non-elastic range, the so-called 'dilatancy' (e.g., [19-20]). As shown by direct observation, dilatancy is caused by the formation and opening of cracks preferentially oriented parallel to the maximum compressive load. This phenomenon introduces a component of radial strain that tends to expand the sample, in competition with the elastic contraction caused by the applied compressive loading. The magnitude of the dilatant component and the conditions under which it occurs cannot yet be given unambiguously---suffice to say, however, no dilatancy is allowed in the present model (see, e.g., expressions (28) and (29)).

*3.3 Dynamic behavior*

As we show in the text, dynamic moduli can be considered elastic. The expressions for Young's modulus $< \tilde{E} >$ and rigidity $< \tilde{G} >$, given by (19) and (21) respectively, depend upon only the elastic properties of the solid matrix material and $\lambda\alpha_j$, the parameter that describes the pore phase. Note that the geometrical characteristics (i.e., $\lambda\alpha_j$) of the joints are explicitly incorporated for in our model, which differs from numerical programs such as 3DEC in simulating cracked rock. The area of the pore phase (here taken to be half of the wetted area) can be found by direct measurements (e.g., [14]). The roughness parameter, defined by (4), can be measured for macroscopic surfaces (e.g., [5], [21]). But in analyses like this one here, $\lambda$ must be considered a geometric property, which always occurs in the product $\lambda\alpha_j$, and which has application only as a term that shows the difference between properties of a porous body and those of the elastic, solid matrix, as in (19), (21), and (24).

The parameter $\lambda\alpha_j$ is non-dimensional. It is useful only if the value found for one physical parameter can then be used to estimate the effect of porosity on another parameter. We find that $\lambda\alpha_j$ can be used in this way. Stewart et al. [22] carried out a series of experiments on Berea sandstone samples, measuring P- and S-wave velocities and attenuation as a function of strain amplitude and confining pressure. We have taken their velocity data and converted them to moduli following standard procedure.

We see in (21) that the slope $s_G$ of a plot of $1/\tilde{G}$ vs. $1/p_0$ can be used to find the porosity parameter $\lambda\alpha_j$; i.e.,

$$s_G = d(1/\tilde{G})/d(1/p_0) = 2\lambda\alpha_j/3 \qquad (36)$$

The slope $s_G$ from Stewart et al. [22] velocity measurements is plotted in Fig. 10. Note that $s_G$ approached a constant value, as predicted by the model, only at pressures above approximately 20 MPa. The lack of agreement at low confining pressure is not surprising, as we discussed

above, the model predicts that moduli are zero when confining pressure is zero, whereas the modulus is finite at all pressures for all rocks because of the tensile strength. Walsh and Grosenbaugh [4] corrected this problem by introducing a term that made the modulus finite at zero pressure; however, this procedure cannot be applied here because it contaminates the behavior of the model as faulting is approaching---i.e., the region of primary interest in this study.

The slope $s_G$ at pressures above 20 MPa is $1.9 \times 10^{-4}$, and so from (36) the parameter $\lambda \alpha_j$ is approximately $3 \times 10^{-4}$. Walsh and Grosenbaugh [4], using measurements of bulk modulus for Navajo sandstone, Casco granite and Westerly granite, found values of $\lambda \alpha_j$ in the range $10^{-4}$ to $10^{-3}$, depending upon rock type and measurement technique. Although Berea sandstone was not part of their study, the values of $\lambda \alpha_j$ are in the range expected from our analysis.

As discussed above, the parameter $\lambda \alpha_j$ must be applicable to other properties that depend on porosity. Comparison of (19) and (21) indicate that the slope $s_G$ in (36) must be twice the slope $s_E$ of a plot of $1/\tilde{E}$ vs. $1/p_0$, where

$$s_E = d(1/\tilde{E})/d(1/p_0) = \lambda \alpha_j / 3 \qquad (37)$$

We have plotted the ratio $s_G/s_E$ in Fig. 11. This ratio has the asymptotic value $s_G/s_E = 2$, in agreement with the predicated value, except at low confining pressure where the model is not expected to be accurate.

Measurements of $Q^{-1}$ by Stewart et al. [22] provide another way to estimate the value of $\lambda \alpha_j$. The estimate inevitably lacks precision because it relies on observations of both the pressure dependence of Young's modulus and the dependence of the quality factor on pressure and strain amplitude. Further, measurements of quality factor show that $Q^{-1}$ is proportional to strain amplitude only at amplitudes greater than $10^{-5}$ (see [22] for reference to their measurements). We

have sidestepped this problem by using the rate of change of these elastic and inelastic parameters with pressure rather than measurements of the parameters themselves. Specifically, we calculated $(dQ^{-1}/dp)_{\varepsilon_1}$ and $d(\tilde{E}/p_0)^2/dp$ as a function of pressure and strain amplitude. As shown by (24) the ratio should lead to an estimate of $\lambda\alpha_j$; that is

$$(dQ_E^{-1}/dp)_{\Delta\varepsilon_1}/[d(<\tilde{E}>/p_0)^2/dp] = \frac{4}{3\pi}\Delta\tilde{\varepsilon}_1\lambda\alpha_j F(\beta_\upsilon) \tag{38}$$

where we have made the approximation $(2-\nu)/(2-2\nu)\approx1$. The ratio is plotted in Fig. 12 as a function of strain amplitude and confining pressure. The relationship is approximately linear, as predicted. Confining our attention only to data at higher pressures, for the reasons discussed above, we see that the slope is approximately $3.6\times10^{-5}$; that is, from (38)

$$\lambda\alpha_j = 3.6\times10^{-4}(\frac{3\pi}{4})F(\beta_\upsilon)^{-1} \tag{39}$$

If we use a friction coefficient $f$ of 0.6---the value commonly used for sliding polycrystalline rock surfaces, the porosity parameter $\lambda\alpha_j$ is approximately $2\times10^{-3}$. On the other hand, measurements by Byerlee and by Horne and Deere (e.g. [23]) suggest that a friction coefficient in the range 0.1-0.2 is appropriate for very low amplitude displacements and for sliding between single crystal materials. Using a friction coefficient of 0.2, we find that $\lambda\alpha_j$ is approximately $4\times10^{-4}$. We see that both values of $\lambda\alpha_j$ are consistent with the values obtained using expressions for elastic moduli.


**Conclusion**

A new model was utilized to study the constitutive behavior of rock under axially-symmetric loading. In this model, the pore phase is approximated by rough planes, randomly spaced and oriented, extending through the sample. The roughness is caused by asperities, and

we assume that all asperities have the same tip radius $R$ and the distribution g($h/\lambda$) of asperity heights $h$ is given by a negative exponential $e^{-h/\lambda}$. Slip at contacts under local shear stress is resisted by simple Coulomb friction, with friction coefficient $f$.

1. Using this model, we derived general expressions of stress-strain relations in terms of the non-dimensional parameter $\lambda\alpha_j$ that describes the configuration of the pore phase, the friction coefficient $f$, and the ratio $r$ of the applied radial stress $\Delta\sigma_3$ to the axial value $\Delta\sigma_1$.

2. Our model provides a quantitative approximation to the brittle failure process. In our model, stress-induced microfracturing begins as randomly oriented microslip throughout the sample. As axial load increases, microslip occurs along preferred orientation and location, which finally leads to deformation on a single fault. The model was found to fault under static loading conditions---the axial load at faulting and the angle of the "fracture" plane agree with values of those parameters given by Coulomb's theory of fracture.

3. We demonstrated that the dynamic moduli and Poisson's ratio are virtually elastic and independent of the friction coefficient acting at contacts.

4. We also demonstrated that the attenuation $Q_E^{-1}$ for uniaxial dynamic loading is a strong function of the friction coefficient and increases linearly with strain amplitude, in agreement with laboratory measurements.

The constitutive relations derived from our model are based on Greenwood and Williamson [6] and Walsh and Zhu [5]. It is shown that the results from our model are consistent with Coulomb's theory of fracture and agree well with existing experimental data. Our model provides a useful tool in studying the response of a rock mass where joints or fractures are well-developed [e.g., 25]. While the numerical modeling becomes a standard tool to determine stress-

states and elastic properties of a complex structure, our model should provide a necessary ground truth for increasingly intricate multi-dimensional, multi layered computer programs.

# References

[1] Brace, WF, Orange, AS, Madden, TR. The effect of pressure on the electrical resistivity of water-saturated crystalline rocks. J Geophys Res 1965; 70:5669-5678.

[2] Walsh, JB. The effect of cracks on the compressibility of rocks. J Geophys Res 1965; 70:381-389.

[3] Jaeger, JC, Cook, NGW. Fundamentals of Rock Mechanics, 3$^{rd}$ Edition. Chapman & Hall: London; 1979.

[4] Walsh, JB, Grosenbaugh, MA. A new model for analyzing the effect of fractures on compressibility. J Geophys Res 1979; 84:3532-3536.

[5] Walsh, JB, Zhu, W. Sliding of a Rough Surface Under Oblique Loading, J Geophys Res 2004; 109:doi:10.1029/2004JB003027.

[6] Greenwood, JA, Williamson, JBP. Contact of nominally flat surface. Proc R Soc Lond A 1966; 295:300-319.

[7] Walsh, JB. A theoretical analysis of sliding of rough surfaces, J Geophys Res 2003; 108: doi: 10.1029/2002JB002127.

[8] Love, AEH. A Treatise on the Mathematical Theory of Elasticity, 4$^{th}$ edition. Cambridge University Press: Cambridge; 1927.

[9] Mindlin, RD, Deresiewicz, H. Elastic spheres in contact under varying oblique forces. J Appl Mech 1949; 16:259-268.

[10] Cartwright, DE, Longuet-Higgins, MS. The statistical distribution of the maxima of a random function. Proc R Soc London A 1956; 237:212-232.

[11] Longuet-Higgins, MS. The statistical analysis of a random moving surface. Phil Trans R Soc London A 1957; 249:321-387.

[12] Nayak, PR. Random process model of rough surfaces. J Lubr Technol 1971; 93:398-407.

[13] Gradsteyn, IS, Ryzhik, IM. Tables of Integrals Series and Products. Academic Press, New York, 1965.

[14] Wong, Tf, Fredrich, JT, Gwanmesia, GD. Crack Aperture Statistics and Pore Space Fractal Geometry of Westerly Granite and Rutland Quartzite: Implications for an Elastic Contact Model of Rock Compressibility. J Geophys Res 1989; 94:10,267-10,278.

[15] Handin, J, Hager, RV, Friedman, M, Feather, JN. Experimental deformation of sedimentary rock under confining pressure: pore pressure effects. Bull Am Ass Petrol Geol 1963; 47:717-755.

[16] Brace, WF, Paulding, BW, Scholz, CH. Dilatancy in the fracture of crystalline rocks. J Geophys Res 1966; 71:3939-3953.

[17] Wong Tf, David, C, Zhu, W. The transition from brittle faulting to cataclastic flow in porous sandstones: Mechanical deformation. J Geophys Res 1997; 102:3009-3025.

[18] Lockner, DA, Byerlee, JD, Kuksenko, V, Ponomarev, A, Sidorin, A. Observations of quasistatic fault growth from acoustic emission. In: Evans B, Wong Tf, editors. Fault Mechanics and Transport Properties of Rocks. Academic Press: San Diego; 1992 p. 1-31.

[19] Brace, WF, Walsh, JB, Frangos, WT. Permeability of granite under high pressure. J Geophys Res 1968; 73:2225-2236.

[20] Fredrich, JT, Evans B, Wong, Tf. Micromechanics of the brittle to plastic transition in Carrara Marble. J Geophys Res 1989; 94:4129-4145.

[21] Brown, SR, Scholz, CH. Closure of rock joints. J Geophys Res 1986; 91:4939-4998.

[22] Stewart, RR, Toksoz, MN, Timur, A. Strain dependent attenuation: Observations and a proposed mechanism. J Geophys Res 1983; 88:546-554.

[23] Byerlee, J. Friction of rocks. Pure Appl. Geophys 1978; 116:615–626.

[24] Johnson, KL. Contact Mechanics. Cambridge University Press; Cambridge: 1987. p93.

[25] Brady, HG, ML Cramer, and RD Hart, Preliminary analysis of a loading test on a large basalt block. Int. J. Rock Mech. Min. Sci. & Geomech. Abstr. 1985; 22: 345-348.

**Figure Caption**

Fig. 1. In the model (having dimension LxLxL), the linearly elastic matrix is intersected by rough joints, randomly distributed and oriented. The load ($\sigma_1$, $\sigma_2$, $\sigma_3$) is axially symmetric ($\sigma_1 \geq \sigma_2 = \sigma_3$).

Fig. 2. a) An arbitrary plane in the sample is oriented at angle to the axial load $\sigma_1$. Because of the axial symmetry of the loading system, we can consider only planes parallel to $\sigma_3$. b) Stress $\sigma_3$ parallel to the plane has no effect on deformation of the joint, and so only $\sigma_1$ and $\sigma_2$ must be included in the analysis. Note in the figure that ($\sigma_1$, $\sigma_2$) cause normal and shear stresses ($\sigma_c$, $\tau_c$) at contacts.

Fig. 3. The applied loading system is a hydrostatic confining pressure $p_0$ (not shown) with a superposed axial stress difference $\Delta\sigma_1$ ($=\sigma_1 - p_0$) and a radial stress difference $r\Delta\sigma_1$ where $r$ is a proportionality constant. These stresses are equilibrated by shear stress $\tau$ and normal stress $\Delta\sigma$ ($=\sigma - p_0$) difference acting on the joint plane.

Fig. 4. The contribution of deformation of a representative rough surface to overall deformation is found using the Reciprocal Theorem. Applying the Reciprocal Theorem requires consideration of two bodies having the same configuration and elastic properties, as in a) and b) in the figure (see text for details). In a), applying ($\Delta\sigma_1$, $\Delta\sigma_3$) causes axial and radial deformations ($\Delta u_1$, $\Delta u_3$) of the body as a whole. In b) applied external loads ($\Delta\sigma_1$, $\Delta\sigma_3$) are equilibrated by internal load ($\Delta\sigma_1$, $\Delta\sigma_3$) acting on the joint surface. The entire body in b) is therefore under a

uniform state of stress ($\Delta\sigma_1$, $\Delta\sigma_3$), and so overall displacements ($\Delta u_a{}^M$, $\Delta u_r{}^M$) are those for an elastic body.

Fig. 5. Axial and radial displacement components ($\Delta u_1$, $\Delta u_3$) acting on the fault are rotated to components ($\Delta u$, $\Delta w$) parallel and normal to the fault surface.

Fig. 6. To insure randomness, planes are considered to be uniformly distributed on the surface of a unit sphere with the usual polar coordinates ($\varphi$, $\beta$).

Fig. 7. Constitutive behavior, both axial and radial strains ($\varepsilon_a$, $\varepsilon_r$) as a function of axial stress difference $\Delta\sigma_1$ ($=\sigma_1-p_0$), as calculated from (15) using MATHEMATICA. The parameter $f$ is the Coulomb friction coefficient at contacts between the rough surfaces, and $r$ is the ratio between the radial and axial stress differences ($r=\Delta\sigma_3/\Delta\sigma_1$,).

Fig. 8. Brittle failure of a rock. Marked with (*), the failure process can be divided into 4 phases: 1) the elastic phase 0-1, which can be modeled by letting the friction coefficient become infinite; 2) the microfracturing phase 1-2, when the friction coefficient takes a finite value ($f$=0.6 is shown here); 3) the preferential microslip phase 2-3, when slip preferentially occurs along the future plane of faulting; 4) the faulting phase 3-4, when sliding along a single fault occurs. With frictional coefficient $f$=0.6, our model predicts that the faulting angle is ~30°, consistent with Coulomb's theory of fracture. Notice that the actual stress-strain curve of a rock (dashed curve) deviates from our model because of the existence of cohesion. The stress-strain curve of a single fault is from Walsh and Zhu [2004].

Fig. 9. $F(\beta_\upsilon)$ from equation (22) as a function of frictional coefficient $f$.

Fig. 10. Dependence of the slope $s_G = \mathrm{d}(1/\tilde{G})/\mathrm{d}(1/p_0)$ on confining pressure. Shear modulus $\tilde{G}$ was obtained from the S-wave velocity measurements by Stewart et al. [1983] (see their Fig. 5).

Fig. 11. The ratio between two slopes $s_G/s_E$ as a function of confining pressure $p_0$. Shear modulus $\tilde{G}$ and Young's modulus $\tilde{E}$ were obtained from the S and P-wave velocity measurements by Stewart et al. [22], respectively (see their Fig. 5). At high confining pressure, $s_G/s_E \approx 2$, which is consistent with our model predictions. The dashed lines represent large uncertainty in [22] measurements at low confining pressure. Because we did not include tensile strength at zero pressure in our model, we cannot accurately predict mechanical behavior of rocks at low confining pressure.

Fig. 12. The ratio $(dQ^{-1}/dp)_{\varepsilon_1} / d(\tilde{E}/p_0)^2 / dp$ as a function of strain increments at confining pressures $p_0 = 12$ and 20 MPa, respectively. The attenuation data are from Fig. 9 of Stewart et al. [1983].

# APPENDIX

Mindlin and Deresiewicz [9] show that energy $\delta W_F$ lost at the interface between a single asperity loaded by a small alternating force oriented at an angle $\beta$ to the plane of contact is

$$\delta W_F = \frac{(2-\nu)\Delta \tilde{T}^3}{72 G N_0 a_0 f}(1 - f^2 \tan^2 \beta) \qquad \text{(A-1)}$$

where $N_0$ is the normal force, and $\Delta \tilde{T}$ is the tangential component of the oscillating load, both acting on a contact having nominal radius $a_0$; other parameters are defined in the text. Mindlin and Deresiewicz's expression is twice (A-1) because they consider two asperities in contact whereas here we consider a single asperity in contact with a rigid surface.

Mindlin and Deresiewicz [9] show that the compliance of a contact is given by the expression

$$\frac{\Delta \tilde{u}}{\Delta \tilde{T}} = 16 G a_0 / (2 - \nu) \qquad \text{(A-2)}$$

The deformation ($h$-$w$) of the tip of a spherical asperity having tip radius $R$, height $h$ relative to a reference plane that has advanced a distance $w$ is related to contact radius $a_0$ (see [24]) by

$$a_0 = 2R(h - w) \qquad \text{(A-3)}$$

Hertz (see [24]) shows that the force $N_0$ required to produce displacement ($h$-$w$) is given by

$$N_0 = (8\sqrt{2}/3)\sqrt{R}(h - w)^{3/2} E /(1 - \nu^2) \qquad \text{(A-4)}$$

Combining (A-1) through (A-4) gives

$$\delta W_F = C_1 (h - w)^{-1/2}$$

where

$$C_1 = (128 / 3\sqrt{2})(G^2 / E)\sqrt{R}\Delta\tilde{u}^3 (\frac{1 - f^2 \tan^2 \beta}{f})\frac{(1 - v^2)}{(2 - v)^2} \qquad \text{(A-5)}$$

The expression (A-5) giving the energy lost at a single contact must be summed over all contacts to find the energy lost for a rough plane. The probability density distribution $g(h)$ for asperity height can be assumed to be given by the negative exponential

$$g(h / \lambda) = e^{-h/\lambda} \qquad \text{(A-6)}$$

where $\lambda$ is a characteristic length chosen so (A-6) approximates the actual probability when that is known; carrying out this summation, we find the energy $\delta W_F$, per unit area, for a rough plane, is

$$\delta W_F = nC_1 \int_{w/\lambda}^{\infty} (h - w)^{-1/2} e^{-h/\lambda} d(h/\lambda) = nC_1 e^{-w/\lambda}\Gamma(1/2) \qquad \text{(A-7)}$$

where $n$ is the number of asperities per unit area.

The total normal stress $p_0$ acting on the plane is found by summing the forces $N_0$ at individual contacts in (A-4); we find

$$p_0 = nC_2 \int_{w/\lambda}^{\infty} (h - w)^{3/2} e^{-h/\lambda} d(h/\lambda) = nC_2 e^{-w/\lambda}\Gamma(5/2) \qquad \text{(A-8)}$$

where $C_2 = (8\sqrt{2} / 3)\sqrt{R}E / (1 - v^2)$.

Combining (A-7) and (A-8) gives an expression for energy $\delta W_F$:

$$\delta W_F = C_3 \left( \frac{1 - f^2 \tan^2 \beta}{f} \right)\Delta\tau^3$$

where

$$C_3 = (4/3)\lambda p_0^{-2}(2 - v) / (2 - 2v) \qquad \text{(A-9)}$$

Displacement $\Delta\tilde{u}$ is related to the shear load $\Delta\tilde{\tau}$ acting on the plane (see [6]) for $\Delta\tilde{\tau} << p_0$ by the expression

$$\Delta\tilde{u} / \lambda = (\Delta\tilde{\tau} / p_0)(2 - v) / (2 - 2v) \qquad \text{(A-10)}$$

and $\Delta\tilde{\tau}$, in turn, is related to the applied axial load $\Delta\tilde{\sigma}_1$:

$$\Delta\tilde{\tau} = \Delta\tilde{\sigma}_1 \sin\beta\cos\beta \tag{A-11}$$

Combining (A-9), (A-10) and (A-11) gives

$$\delta W_F = C_4 \sin^3\beta\cos^3\beta(1 - f^2\tan^2\beta)/f$$

where

$$C_4 = (4/3)[(2-\nu)/(2-2\nu)](\Delta\tilde{\sigma}_1^3/p_0^2)\lambda \tag{A-12}$$

To find the total energy $\Delta W_F$ dissipated, we must sum the loss for an individual plane, given by (A-12), over the unit sphere, including only those orientations for which loss occurs; that is

$$\Delta W_F = \int_0^{\beta_\upsilon} \delta W_F \sin\beta\cos\beta d\beta \tag{A-13a}$$

giving

$$\Delta W_F = \delta W_F \alpha_j F(\beta_\upsilon) \tag{A-13b}$$

where

$$F(\beta_\upsilon) = \int_0^{\beta_\upsilon} (1/f)(1 - f^2\tan^2\beta)\sin^4\beta\cos^4\beta d\beta.$$

The integration in (A-13b) was carried out numerically using MATHEMATICA 4.0; the function is plotted as a function of friction coefficient $f$ in Fig. 9.

Attenuation is typically measured using the quality factor $Q$; the quality factor is defined as

$$Q_E^{-1} = (1/2\pi)(\Delta W_F / \Delta W_{SE}), \tag{A-14}$$

where $\Delta W_{SE}$ the maximum strain energy during a cycle, is

$$\Delta W_{SE} = \Delta\tilde{\sigma}_1/2 < E >$$

and $<E>$ is the effective Young's modulus. Combining (A-12), (A-13), and (A-14), we find

$$Q_E^{-1} = (4/3\pi)[(2-\nu)/(2-2\nu)]\lambda\alpha_j(\Delta\tilde{\sigma}_1 < E > / p_0^2)F(\beta_\upsilon) \qquad \text{(A-15)}$$

An equivalent form of (A-15) in terms of the strain amplitude $\Delta\tilde{\varepsilon}_1$, of the harmonic load, is given by the expression

$$Q_E^{-1} = \frac{4}{3\pi}\left[\frac{2-\nu}{2(1-\nu)}\right]\lambda\alpha_j(< E > / p_0)^2\Delta\tilde{\varepsilon}_1 F(\beta_\upsilon) \qquad \text{(A-16)}$$
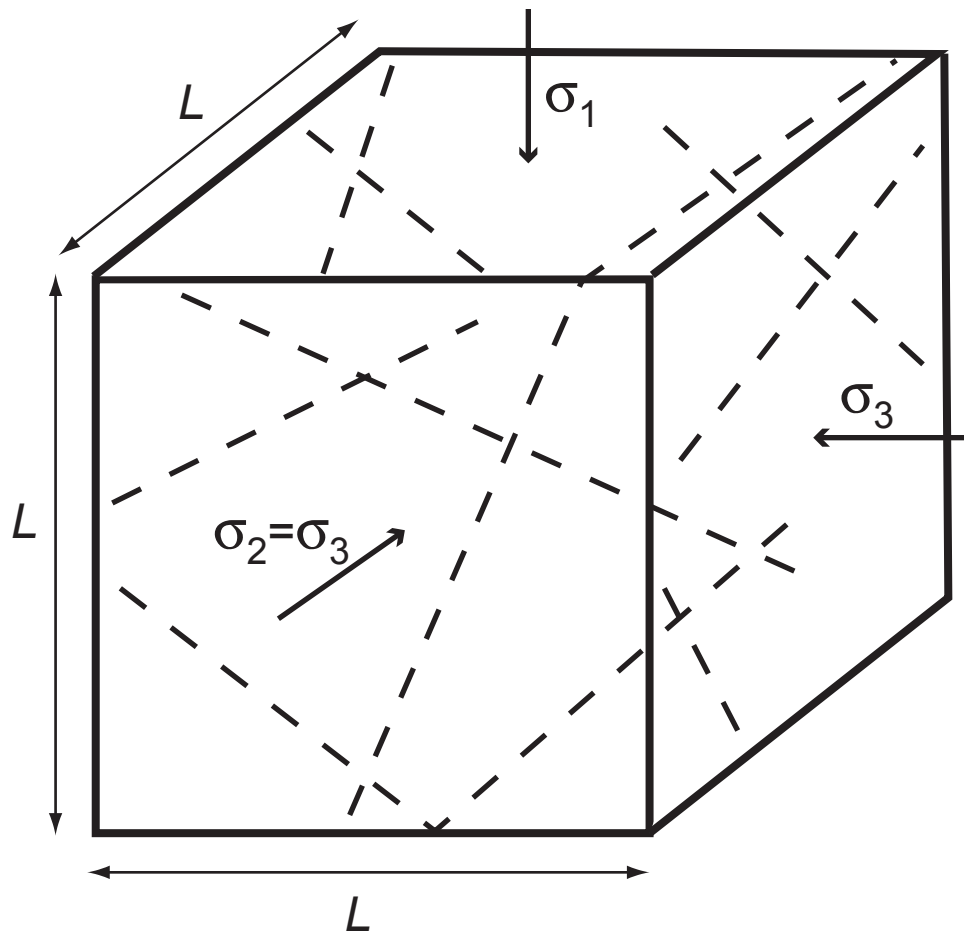
Figure 1

a)
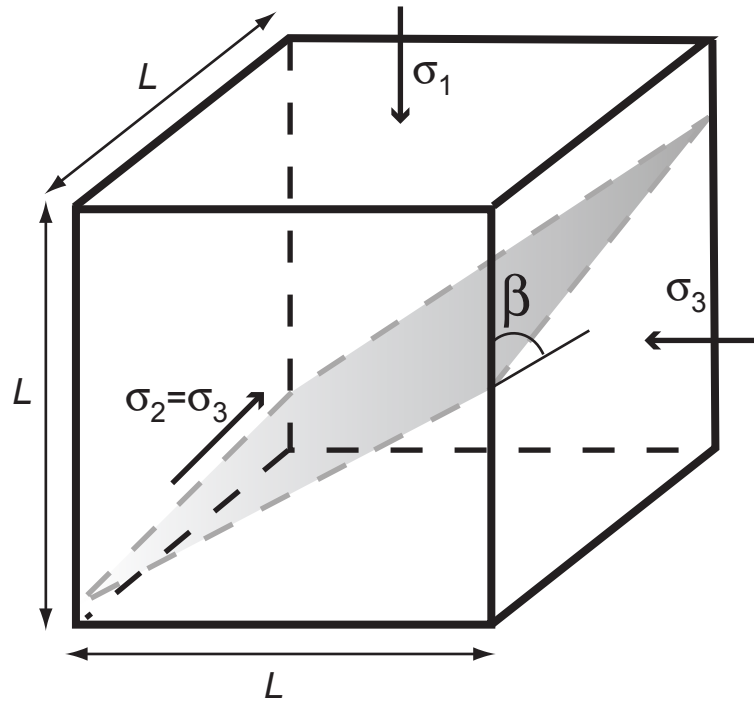
b)

Figure 2

Figure 3

a)

$\Delta\sigma_1$

$\Delta u_a$

$\Delta u_1$

$\Delta u_3$

$\Delta\sigma_3$

$\Delta u_r$

b)

$\Delta\sigma_1$

$\Delta u_a^M$

$\Delta\sigma_3$

$\Delta\sigma_3$

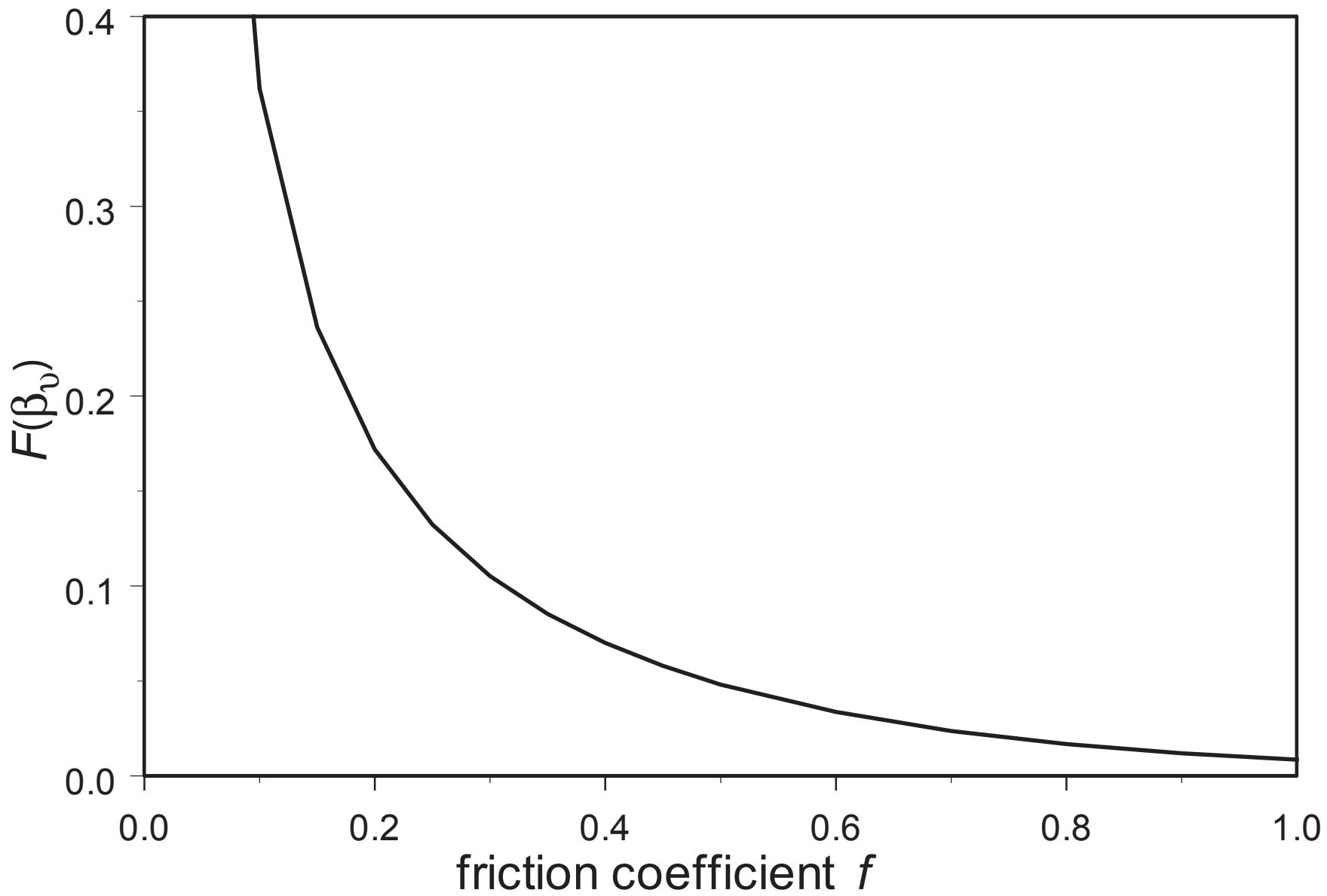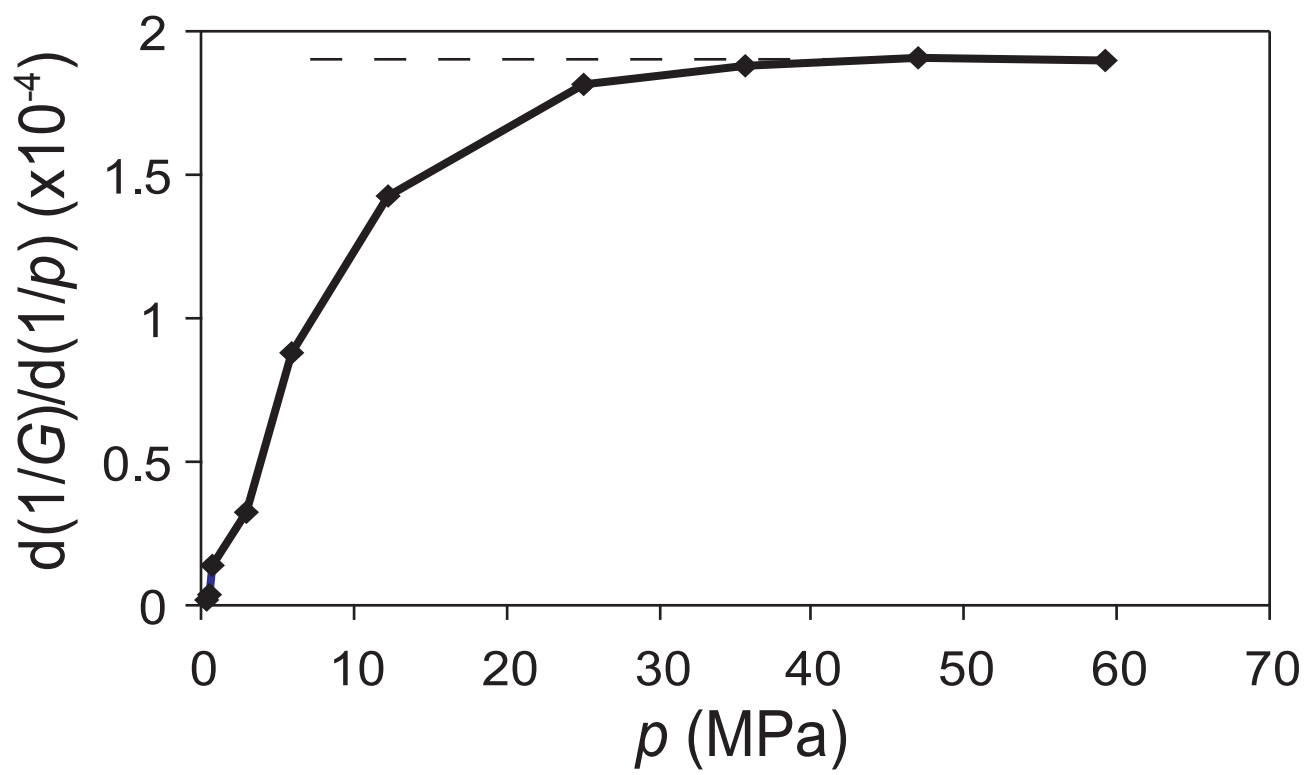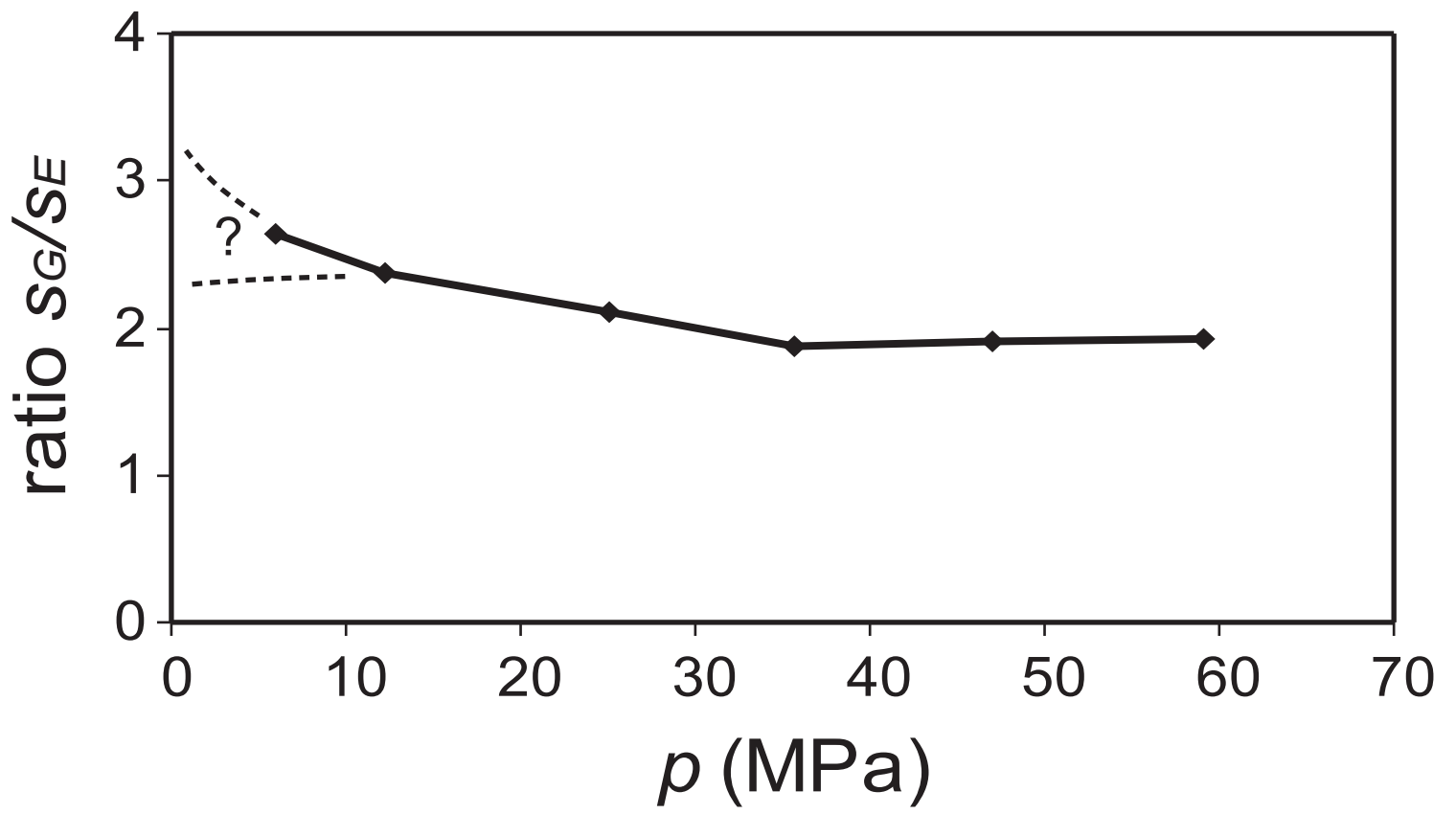$\Delta\sigma_1$

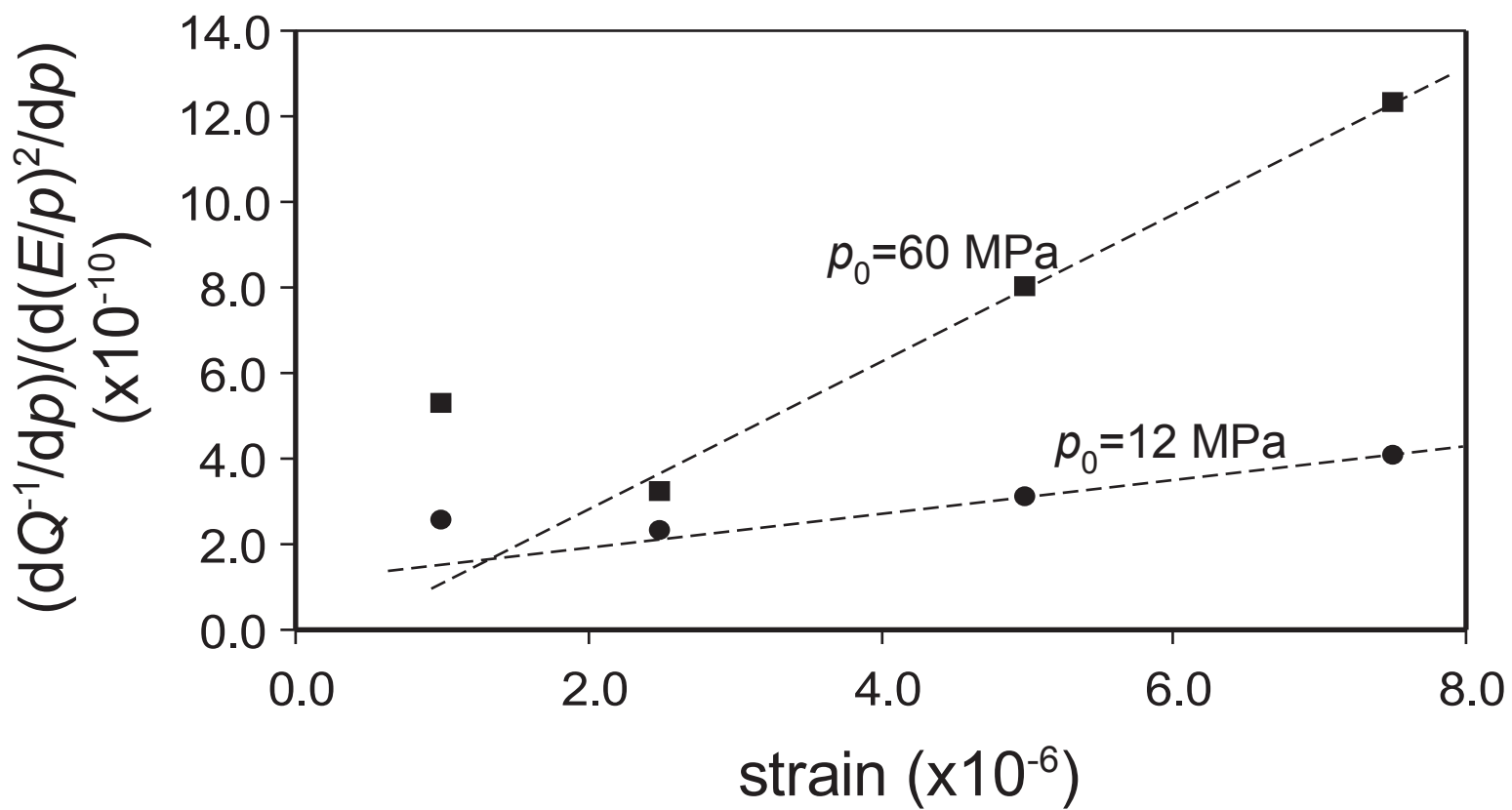$\Delta u_r^M$
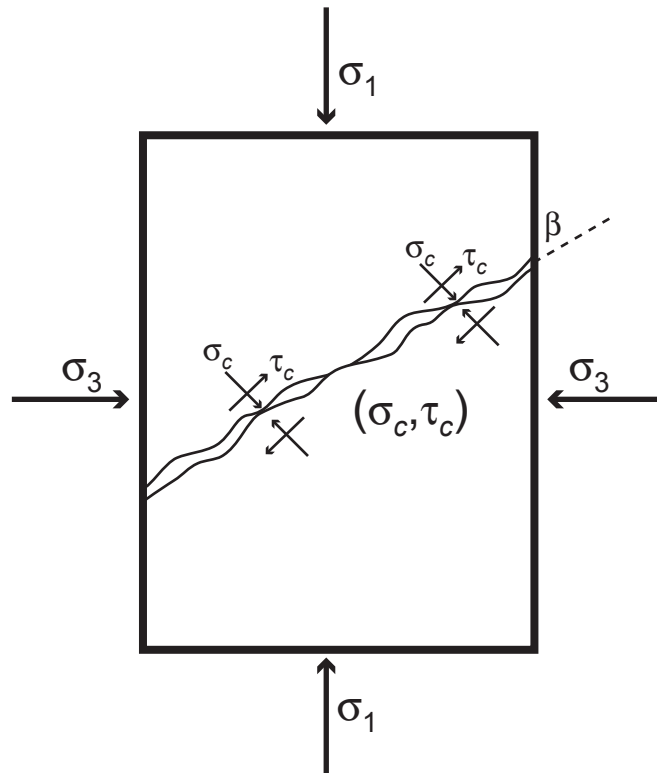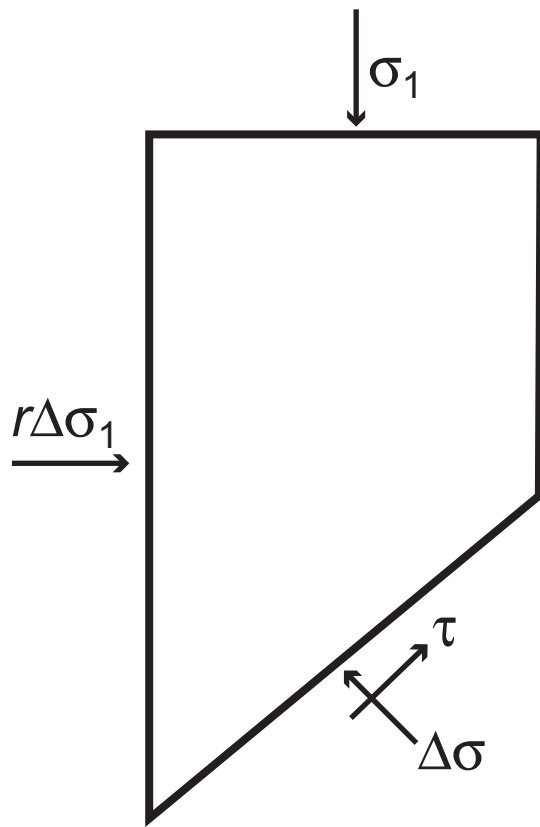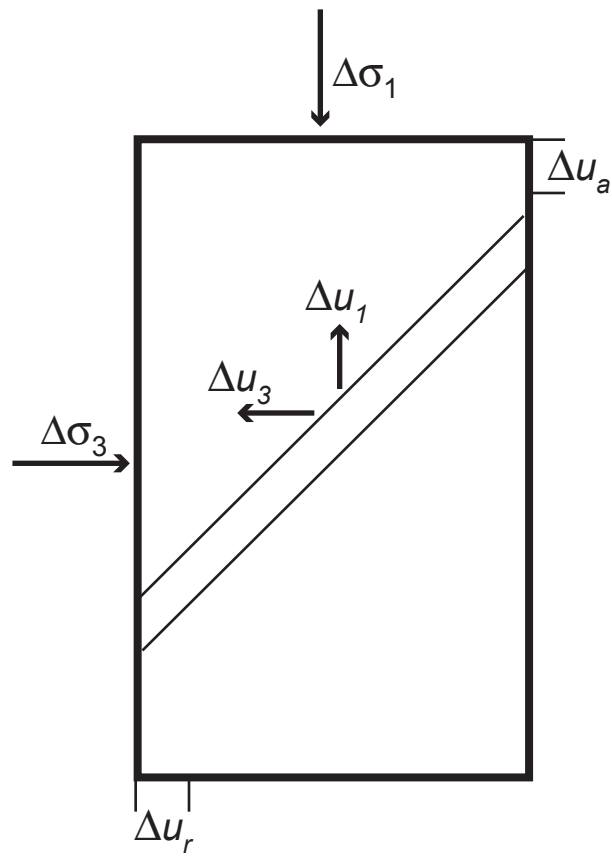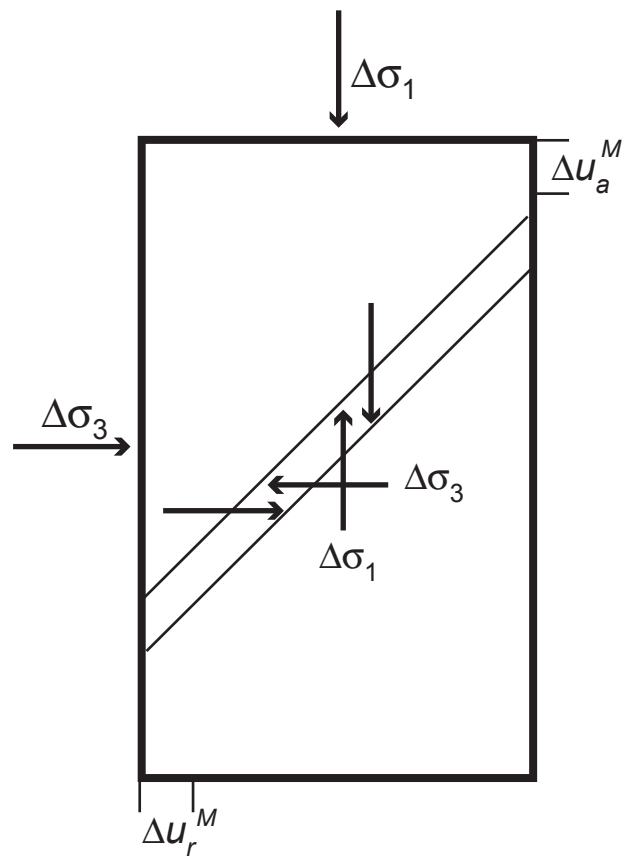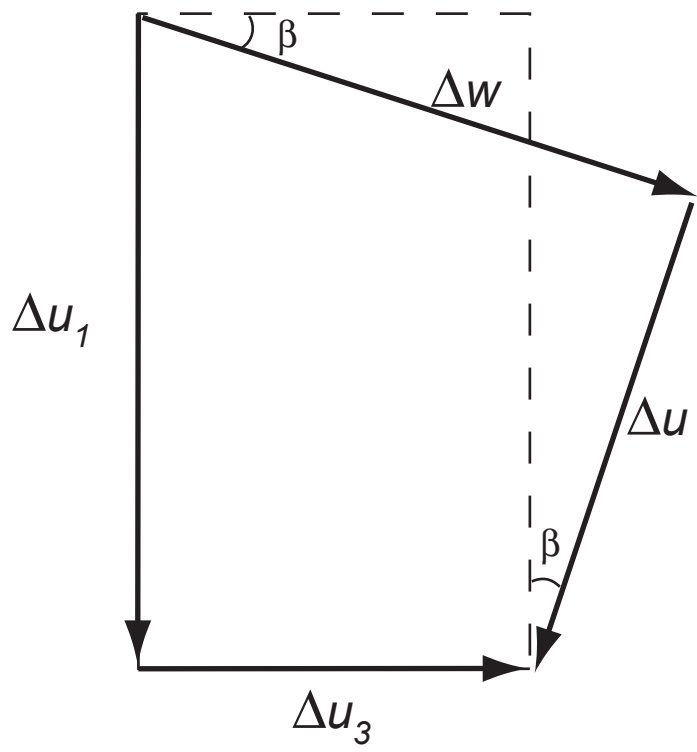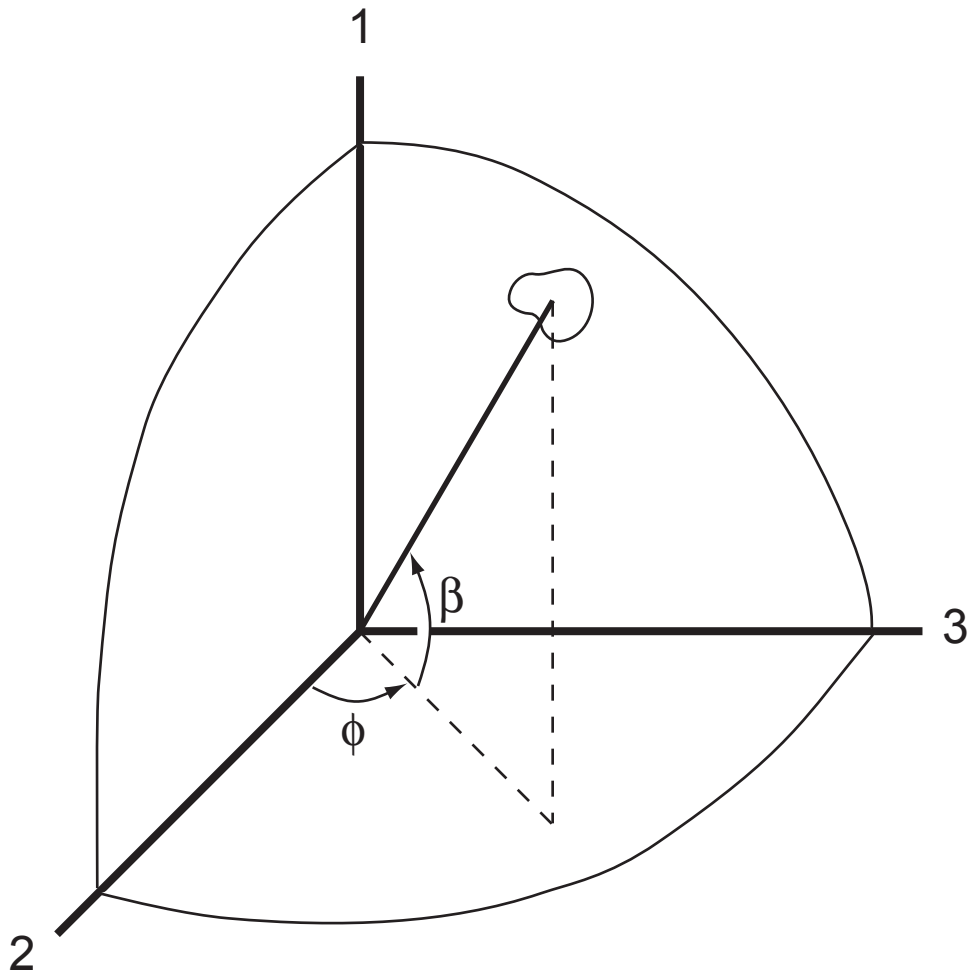
Figure 4

Figure 5

Figure 6
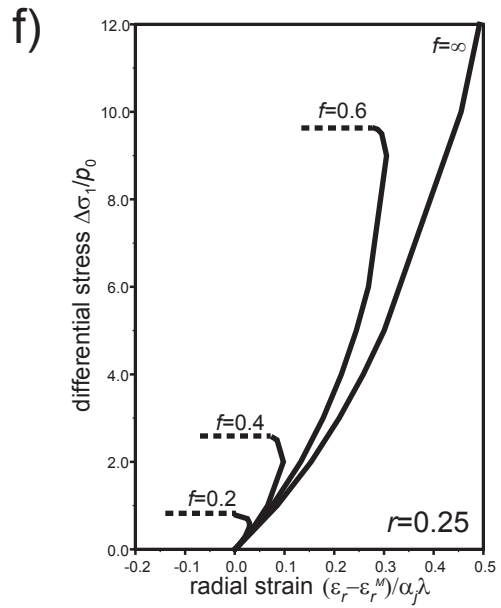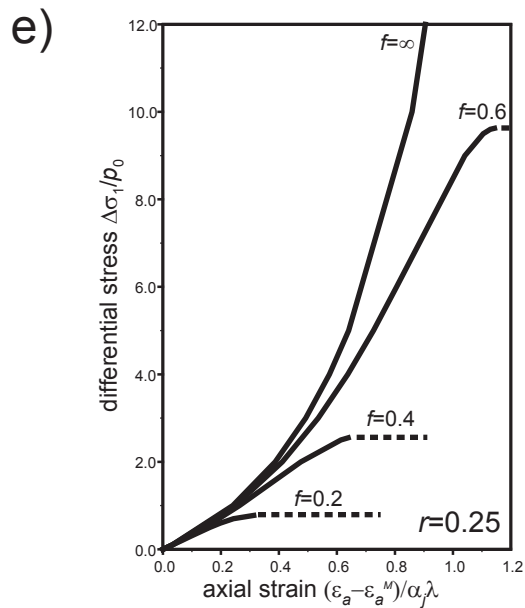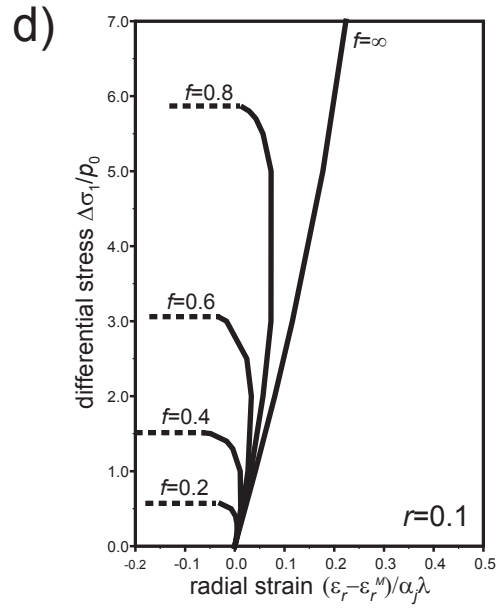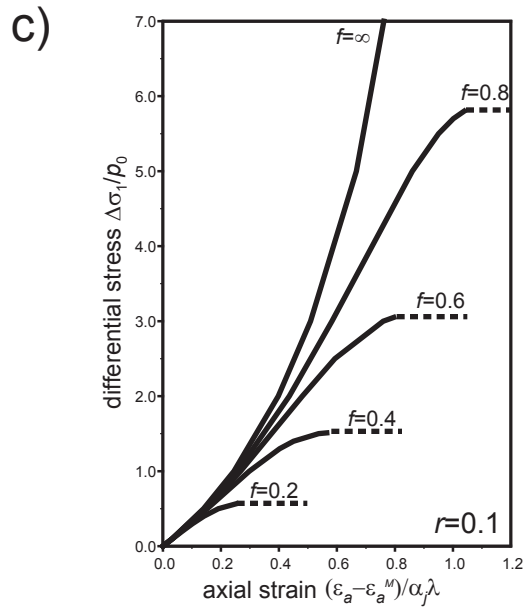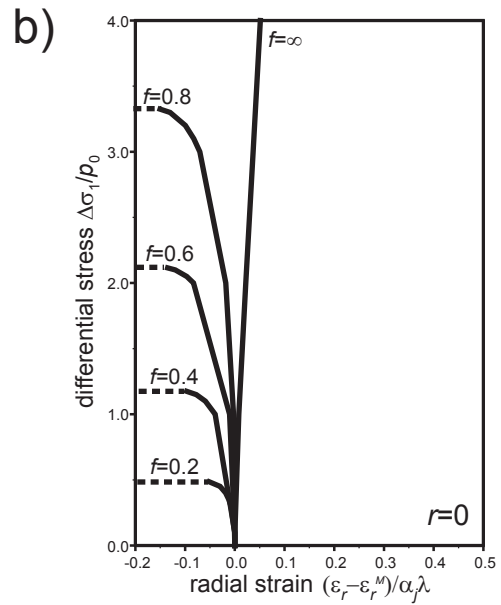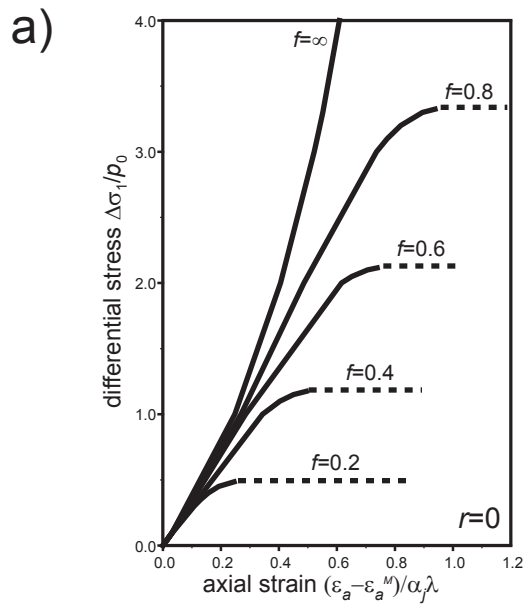
Figure 7
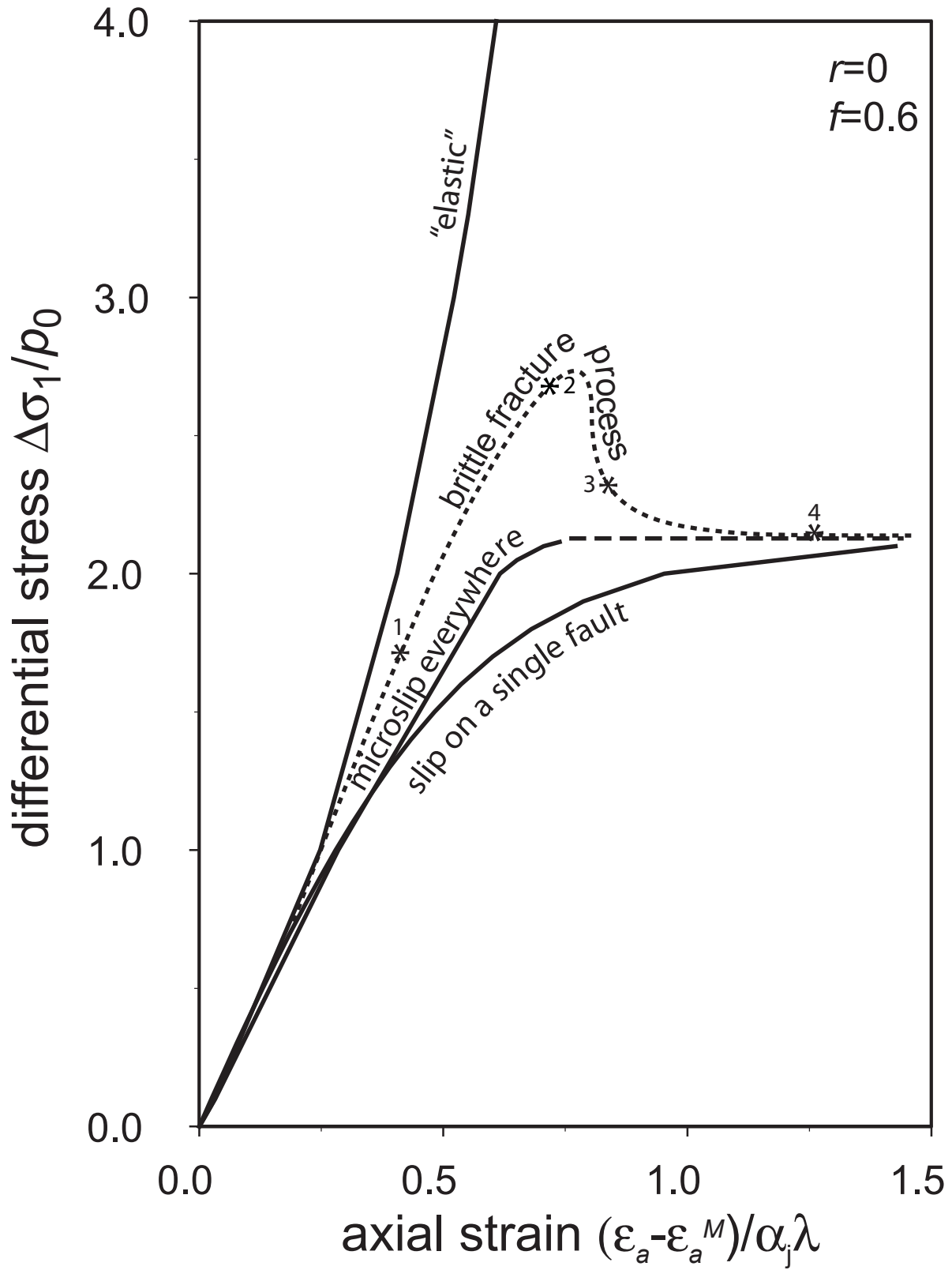
Figure 8

Figure 9

Figure 10

Figure 11

Figure 12